

Io's SO₂ and NaCl Wind Fields From ALMA

ALEXANDER E. THELEN,¹ KATHERINE DE KLEER,¹ MARTIN A. CORDINER,^{2,3}
IMKE DE PATER,⁴ ARIELLE MOULLET,⁵ AND STATIA LUSZCZ-COOK^{6,7}

¹*Division of Geological and Planetary Sciences, California Institute of Technology, Pasadena, CA 91125, USA*

²*Solar System Exploration Division, NASA Goddard Space Flight Center, Greenbelt, MD 20771, USA*

³*Department of Physics, Catholic University of America, Washington, DC 20064, USA*

⁴*Department of Astronomy, Department of Earth and Planetary Science, University of California, Berkeley, CA 94720, USA*

⁵*National Radio Astronomy Observatory, Charlottesville, VA 22903, USA*

⁶*New York University, New York, NY 10003, USA*

⁷*American Museum of Natural History, New York, NY 10024, USA*

ABSTRACT

We present spatially resolved measurements of SO₂ and NaCl winds on Io at several unique points in its orbit: before and after eclipse, and at maximum eastern and western elongation. The derived wind fields represent a unique case of meteorology in a rarified, volcanic atmosphere. Through the use of Doppler shift measurements in emission spectra obtained with the Atacama Large Millimeter/submillimeter Array (ALMA) between ~ 346 – 430 GHz (~ 0.70 – 0.87 mm), line-of-sight winds up to ~ -100 m s⁻¹ in the approaching direction and >250 m s⁻¹ in the receding direction were derived for SO₂ at altitudes of ~ 10 – 50 km, while NaCl winds consistently reached $\sim |150 - 200|$ m s⁻¹ in localized regions up to ~ 30 km above the surface. The wind distributions measured at maximum east and west Jovian elongations, and on the subJovian hemisphere pre- and post-eclipse, were found to be significantly different and complex, corroborating the results of simulations that include surface temperature and frost distribution, volcanic activity, and interactions with the Jovian magnetosphere. Further, the wind speeds of SO₂ and NaCl are often inconsistent in direction and magnitude, indicating that the processes that drive the winds for the two molecular species are different and potentially uncoupled; while the SO₂ wind field can be explained through a combination of sublimation-driven winds, plasma torus interactions, and plume activity, the NaCl winds appear to be primarily driven by the plasma torus.

1. INTRODUCTION

Io, the closest Galilean satellite to Jupiter, harbors a tenuous – but dynamic – atmosphere primarily composed of S-bearing products originating from a combination of surface frost sublimation, volcanic activity, and photodissociation. Atmospheric species can be circulated longitudinally through a cycle of sublimation from and deposition into surface frost during the day and night, respectively (see reviews in [de Pater et al., 2021, 2023a](#)). Additionally, volcanic eruptions can loft gases tens to hundreds of km above the surface at significant (100s m s^{-1}) speeds. Neutral gas escape (e.g., Na, K) leads to the formation of extended gas clouds co-orbiting with Io around Jupiter, while atomic and molecular charge exchange with the Jovian magnetosphere produces ionized species that are accelerated into Io’s plasma torus and distributed throughout the rest of the Jovian system (see [Bagenal & Dols, 2023](#), and references therein). Io’s ionosphere was discovered by the *Pioneer 10* spacecraft ([Kliore et al., 1974](#)), while sulfur dioxide (SO_2) – the primary atmospheric constituent – and volcanic activity were found with *Voyager 1* ([Hanel et al., 1979](#); [Pearl et al., 1979](#); [Morabito et al., 1979](#)). The atmosphere and volcanic features have been subsequently monitored by *Galileo*, *Juno*, and a host of ground- and space-based observations ([Schneider & Spencer, 2023](#)), including recent measurements with the James Webb Space Telescope ([de Pater et al., 2023b](#)). Io’s SO_2 atmosphere was predicted to exhibit latitudinal and longitudinal variability due to the sublimation of inhomogeneously distributed frost, redistribution through pressure driven winds and volcanic outgassing, and convergence on the terminator ([Ingersoll et al., 1985](#); [Ingersoll, 1989](#); [Moreno et al., 1991](#); [Austin & Goldstein, 2000](#); [Moore et al., 2009](#)). Observations have shown that SO_2 is enhanced by up to a factor of ~ 10 on the antiJovian hemisphere compared to the subJovian hemisphere, and mainly confined to $30\text{--}40^\circ$ above and below the equator ([Lellouch et al., 1990](#); [Jessup et al., 2004](#); [Spencer et al., 2005](#); [Feaga et al., 2009](#); [Tsang et al., 2013a](#); [Jessup & Spencer, 2015](#); [Lellouch et al., 2015](#); [de Pater et al., 2020](#); [Giono & Roth, 2021](#)), with evidence for temporal variability between perihelion and aphelion ([Tsang et al., 2012, 2013b](#); [Giles et al., 2024](#)). Volcanic activity can help support the SO_2 atmosphere (particularly when it condenses during eclipses by Jupiter), and can also suffuse additional sulfuric and alkali products – such as NaCl ([Lellouch et al., 2003](#)) and KCl ([Moulet et al., 2013](#)) – into the atmosphere.

While the distribution of Io’s atmospheric species has been observed and modeled throughout the previous decades ([de Pater et al., 2021, 2023a](#)), observations of winds on Io remain sparse. Increasingly sophisticated simulations show the expansion of sublimation-driven winds following atmospheric pressure gradients from the surface location of peak frost temperature, which lags $\sim 10\text{--}30^\circ$ east of the sub-solar point, to Io’s night side ([Walker et al., 2010](#); [de Pater et al., 2020](#)). These flows are complicated by the inclusion of additional atmospheric species ([Moore et al., 2009](#)), surface thermophysical properties ([Walker et al., 2012](#)), localized (and irregular) volcanic outgassing ([McDoniel et al., 2015, 2017](#)), and upper atmospheric interactions with

the plasma torus (Walker et al., 2010; Moore, 2011; Walker, 2012; McDoniel et al., 2019). These processes are depicted in Figure 1.

The resulting wind field may vary with atmospheric species (Moore, 2011; Walker, 2012) – some of which may even manifest cyclonic winds – and undoubtedly with volcanic activity, which varies both spatially and temporally in an unpredictable manner (de Kleer et al., 2019). The predicted pressure gradients across the disk should result in supersonic wind speeds (up to $\sim 500 \text{ m s}^{-1}$ at 10 km; Walker et al., 2012), which may drive circulation around most of the moon within Io’s day ($\sim 42 \text{ hr}$); though yet to be observed, an enhancement of SO_2 gas over the dawn hemisphere (designated as the Dawn Atmospheric Enhancement, or DAE, by Walker et al., 2010) may disrupt the day-to-night flow through the creation of a localized shock front (Figure 1A). Further, the SO_2 atmosphere collapses rapidly (on order minutes) during eclipse (Tsang et al., 2015, 2016; de Pater et al., 2020), possibly precluding a stable flow from being established over complete diurnal timescales. The duration required to rebuild the atmosphere following eclipse is $\sim 10 \text{ min}$, yet the time for winds to achieve measurable speeds due to temperature gradients is predicted to lag on order $\sim 1\text{--}2 \text{ hr}$ (Walker et al., 2012). Thus, variation in wind speeds throughout Io’s day (particularly following eclipses) may be observable. While planetary winds on the terrestrial and Giant planets – and Saturn’s moon, Titan – have been inferred through cloud-tracking observations (see review by Simon et al., 2022, and references therein), stellar occultation measurements (see review by Sicardy, 2023), or through atmospheric temperature fields (*via* the thermal wind equation, e.g., Flasar et al., 2005; Achterberg et al., 2008), none of these techniques are applicable to the atmosphere of Io due to its rarefied nature.

Observations of Io at (sub)millimeter wavelengths previously revealed the distribution of SO_2 , SO , and alkali gases using a variety of single-dish and interferometric facilities (Lellouch et al., 1990, 1992, 1996, 2003; Moullet et al., 2010, 2013; Roth et al., 2020; de Pater et al., 2020; Redwing et al., 2022; de Kleer et al., 2024). Moullet et al. (2008) made the first direct measurements of atmospheric winds in Io’s SO_2 using the Institut de Radioastronomie Millimétrique (IRAM) Plateau de Bure Interferometer (PdBI). These observations showed prograde, super-rotating winds with a $330 \pm 100 \text{ m s}^{-1}$ difference from limb-to-limb on Io’s leading hemisphere ($\sim 90^\circ\text{W}$; eastern Jovian elongation), which were not predicted by prior models of day-to-night sublimation-driven winds. Subsequent line-of-sight wind models by Gratiy et al. (2010) were able to produce a similar limb-to-limb wind magnitude; however, these results showed large ($\sim 300 \text{ m s}^{-1}$) red-shifted velocities at the dusk limb, and minor ($\sim 50 \text{ m s}^{-1}$) blue-shifted velocities at the dawn limb, which were at odds with the relatively evenly distributed red-shifted ($160 \pm 80 \text{ m s}^{-1}$) and blue-shifted ($170 \pm 80 \text{ m s}^{-1}$) winds of the IRAM/PdBI observations (Moullet et al., 2008). Volcanic plume activity and plasma torus momentum transfer could potentially drive the observed apparent prograde flow. However, the low spatial resolution ($\sim 0.5 \times 1.5''$) of the IRAM/PdBI

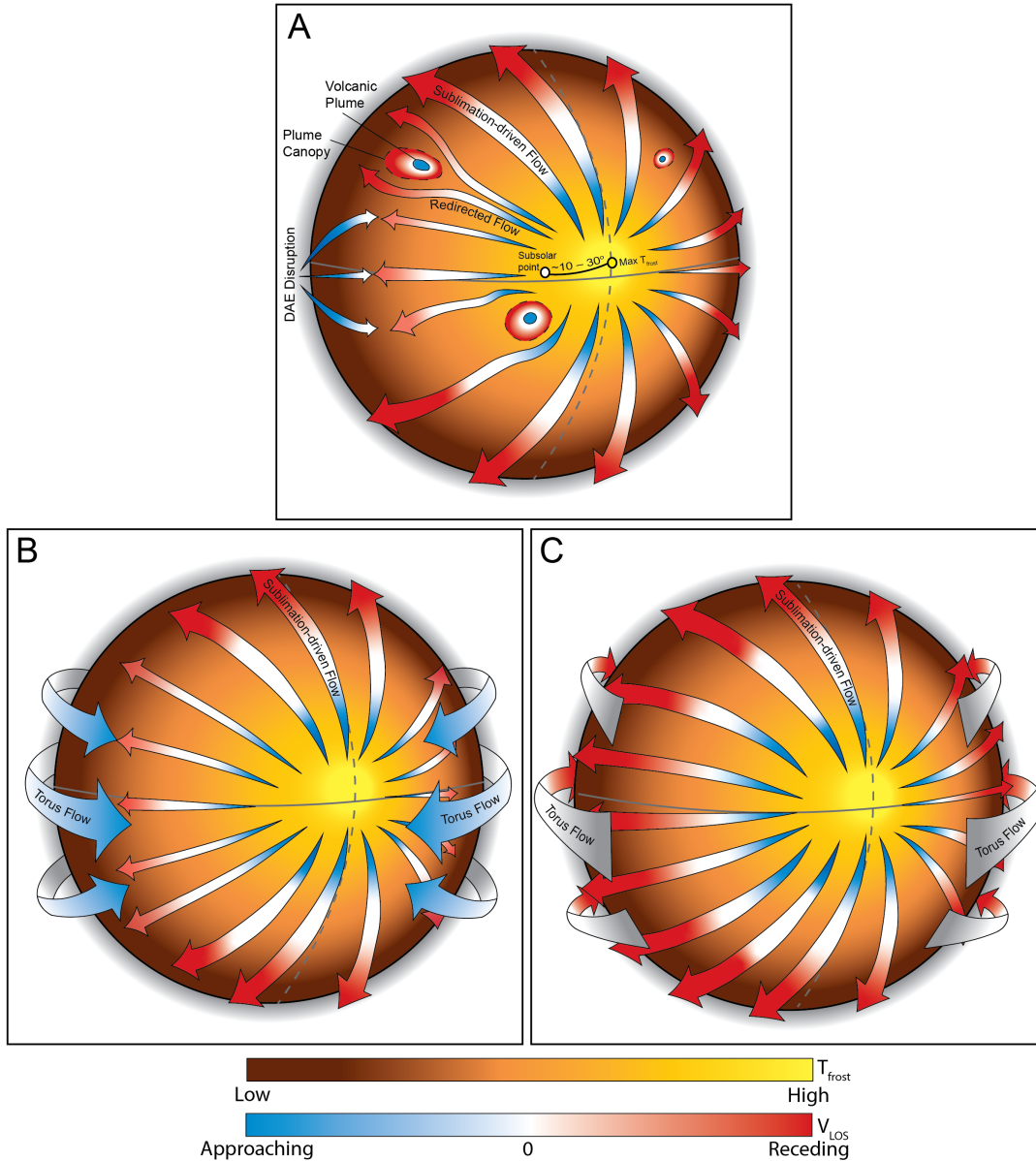


Figure 1. Diagram of Io’s wind field as predicted by models and observable through line-of-sight (LOS) Doppler measurements. (A) Processes driving Io’s wind field without the influence of the plasma torus, including sublimation-driven winds, volcanic plumes and surrounding canopies, and disruption of the day-to-night wind flow by the dawn atmospheric enhancement. Note that volcanic emission will be small compared to the ALMA beam, and the plume sizes are exaggerated for clarity here. (B) Schematic of Io’s leading hemisphere showing the competition of sublimation-driven winds and the plasma torus, which impedes day-to-night flow at the dawn and dusk terminators. (C) Similar to B, but for Io’s trailing hemisphere. Here, the plasma flow enhances the sublimation-driven flow at both terminators. In all panels, the orange color scale reflects the surface SO_2 frost temperature, which is offset from the sub-solar longitude by $\sim 10 - 30^\circ$ (see models by, e.g., Walker et al. 2010, and continuum observations by de Pater et al. 2020). Blue gradients represent LOS winds moving radially towards the observer, while red represents LOS winds moving away from the observer.

observations provided insufficient sampling of the wind field to distinguish between these (and other) mechanisms implemented in wind models.

Recently, the Atacama Large Millimeter/submillimeter Array (ALMA) has enabled higher angular resolution ($<0.5''$) observations in the (sub)millimeter wavelength regime, allowing for the derivation of zonal atmospheric winds on Titan (Lellouch et al., 2019; Cordiner et al., 2020), Jupiter (Cavalié et al., 2021), Saturn (Benmahi et al., 2022), and Neptune (Carrión-González et al., 2023). Here, we measure spatially resolved winds on Io at both maximum eastern and western elongations, and shortly before and after eclipse, utilizing ALMA observations previously obtained for the purposes of investigating atmospheric collapse (de Pater et al., 2020) and measuring isotope ratios of S and Cl in molecular species (de Kleer et al., 2024).

2. OBSERVATIONS

The ALMA facility provides exceptional angular resolution and spectroscopic capabilities through the combination of 40–50 12-m antenna dishes, with receivers that can be tuned to frequencies between 35–950 GHz (~ 0.3 –8.6 mm) at spectral resolutions down to 31 kHz. Together, these capacities facilitate the derivation of Doppler shifts in myriad spectral lines, including the sulfur-bearing (de Pater et al., 2020) and chlorinated (Redwing et al., 2022) species – and their isotopologues (de Kleer et al., 2024) – detected on Io thus far.

For this work, we have chosen three ALMA datasets from ALMA Band 7 (275–373 GHz; ~ 0.8 –1.1 mm) and 8 (385–500 GHz; ~ 0.6 –0.8 mm) consisting of seven individual observations of Io in sunlight; the observing parameters are detailed in Table 1. Observations of Io at both maximum Jovian elongations were acquired on 2021 July 15 and 23. These observations were reduced in a similar manner to previous studies (de Pater et al., 2020; de Kleer et al., 2024), using the scripts provided by the ALMA Observatory in the Common Astronomy Software Analysis (CASA) package (McMullin et al., 2007; CASA Team et al., 2022). For the purposes of this study, multiple ALMA integrations on Io over a period of ~ 4.5 hr were combined so as to improve the spectral signal-to-noise ratio (SNR). The approximate sub-observer longitudes during the mid-points of these observations were $\sim 98^\circ\text{W}$ and 266°W for the leading and trailing hemisphere observations, respectively, though the integration of multiple ALMA executions over a ~ 4.5 hr period resulted in some longitudinal smearing ($\sim 38^\circ$). We leave the analysis of the individual, shorter (~ 45 min) ALMA scans from these data to future work.

Io’s continuum emission was subtracted from the calibrated ALMA data using the CASA `uvcontsub` task, which operates on the complex visibility measurements obtained through the Fourier transform of Io’s brightness distribution on the sky as observed by each antenna pair. Subsequent image deconvolution was performed using the CASA `tclean` algorithm (Högbom, 1974) with pixel sizes = $0.01''$. This included iterative phase self-calibration, as discussed in de Pater et al. (2020). The

observations were taken with 42 and 45 12-m antennas spatially separated by up to ~ 2.5 km, which resulted in images of Io at a spatial resolution of $\sim 0.1'' \times 0.1''$ when using the Briggs weighting scheme (Briggs, 1995) during deconvolution (robust parameter = 0.5). We further convolved the native ALMA synthesized beam shape (analogous to a point-spread function) from these observations with a second Gaussian function using the CASA `imsmooth` task to achieve a resolution of $0.20'' \times 0.20''$, so as to improve the spectral SNR (and thus the measured velocity SNR) in each pixel and to better facilitate the comparison to other observations.

The data from observations in 2018 and 2022 were utilized directly from the previous analyses by de Pater et al. (2020) and de Kleer et al. (2024), respectively. These data include observations of Io at multiple times throughout its orbit: shortly ($\lesssim 30$ min) before (March) and after (September) eclipse in 2018, and at both eastern and western Jovian elongations in 2022 May. While many SO_2 transitions, as well as those of SO , KCl , and various isotopologues were detected in these observations, we only utilize the strongest two to three SO_2 transitions, and the NaCl ($J = 33 - 32$) transition from the 2022 data, for this study (spectral transitions are tabulated in Appendix A). Imaging of the ALMA data from these projects with pixel sizes of $0.04''$ (2018) and $0.03''$ (2022) produced image cubes with spatial scales of $\sim 0.22\text{--}0.35''$ when performing `tclean` with Briggs weighting (robust = 0.5), which were used again here without further alteration.

In all instances, spectra were obtained with a native spectral resolution of 141 or 282 kHz ($\sim 0.1\text{--}0.2$ km s $^{-1}$), allowing for high precision velocity measurements when fitting a line profile across multiple ($\sim 9\text{--}18$) spectral channels. While additional observations of Io during 2018 exist, these were taken (intentionally) while Io was eclipsed by Jupiter (de Pater et al., 2020). As such, the emission from sublimated SO_2 was significantly reduced due to the rapid collapse of Io’s atmosphere during eclipse (leaving only weak emission from volcanic SO_2 gas), and did not permit the accurate measurement of winds.

The spatial distribution of Io’s atmospheric SO_2 and NaCl is shown for each of these observations in Figure 2, which was obtained by integrating over the spectral line emission in each pixel. The SO_2 and NaCl emission originates from the lower ~ 50 km of the atmosphere as depicted by the contribution functions in de Pater et al. 2020 and de Kleer et al. 2024 (see their Figures 12 and S3, respectively), which depend on the fractional coverage of the gas across the disk, the column density and temperature. As in prior observations of Io in the (sub)millimeter (Moulet et al., 2010; de Pater et al., 2020), IR (Spencer et al., 2005), and UV (Feaga et al., 2009), the SO_2 gas distribution is mostly confined to low latitudes and enhanced on Io’s antiJovian hemisphere at each maximum elongation. A secondary, smaller enhancement is evident on the trailing hemisphere (Figure 2G, H), which may be related to the DAE proposed by Walker et al. (2010). The NaCl emission is highly

Table 1. Observational Parameters

Project Code #	Date	Ang. Dia. ^a (")	Ang. Res. (")	Spec. Res. (kHz [km s ⁻¹])	Lat. (°)	W. Lon. (°)	Refs.
2017.1.00670.S	2018 Mar. 20	1.06	0.35 × 0.35	141 [0.12]	-3.40	337.2	[1]
	2018 Sept. 02	0.89	0.30 × 0.30	141 [0.12]	-2.96	25.3	[1]
	2018 Sept. 11	0.87	0.22 × 0.22	141 [0.12]	-2.95	21.5	[1]
2019.1.00216.S	2021 July 15	1.20	0.20 × 0.20	141 [0.12]	0.86	98.0	
	2021 July 23	1.22	0.20 × 0.20	141 [0.12]	0.86	266.0	
2021.1.00849.S	2022 May 18	0.92	0.30 × 0.27	282 [0.20]	2.09	277.1	[2]
	2022 May 24	0.94	0.35 × 0.23	282 [0.20]	2.14	76.8	[2]

NOTE—^aColumn denotes the angular diameter of Io for each observation. References: [1] [de Pater et al. \(2020\)](#); [2] [de Kleer et al. \(2024\)](#). Data from ALMA Project Code #2019.1.00216.S has not been previously published.

localized, interpreted by previous studies as a tracer of volcanic outgassing ([Redwing et al., 2022](#); [de Kleer et al., 2024](#)).

3. SPECTRAL LINE MODELING & FITTING

Following the acquisition of ALMA spectral line image cubes, the LOS radial velocities across Io were derived by fitting the spectral line shape from each pixel. These velocities were then translated to LOS wind speeds by accounting for the moon’s solid-body rotation (75 m s⁻¹ at the limb), which can be substantial compared to the derived velocities, those previously measured in the millimeter ([Moulet et al., 2008](#)), and predicted by models ([Gratiy et al., 2010](#)). The methods used to derive Io’s wind speeds (and associated uncertainties) follow the procedures described in [Cordiner et al. \(2020\)](#), employed in that study for the measurement of zonal winds in Titan’s upper stratosphere, mesosphere, and thermosphere. Unlike (sub)millimeter molecular emission on Titan and the giant planets, Io’s SO₂ and NaCl lines are not broadened by pressure but only by Doppler thermal broadening and winds ([Lellouch et al., 1990](#); [Gratiy et al., 2010](#)). As such, these spectra were well-fit by a Gaussian line shape. The spectrum extracted from each pixel was fit independently over a ~ 6 –12 MHz (50 spectral channels) region surrounding the spectral line. Starting with the gas temperature, SO₂ and NaCl column densities found by [de Kleer et al. \(2024\)](#) for both leading and trailing hemispheres of Io, a uniform slab model was used to produce model spectra using a Gaussian line shape and varying the gas column density. Here, we assumed local thermodynamic equilibrium based on previously modeled rotational emission in Io’s lower atmosphere ([Lellouch et al., 1992](#); [Gratiy et al., 2010](#); [Walker et al., 2010](#); [de Pater et al., 2020](#); [de Kleer et al., 2024](#)). The `mpfit` module in Python¹

¹ <https://cars9.uchicago.edu/software/python/mpfit.html>

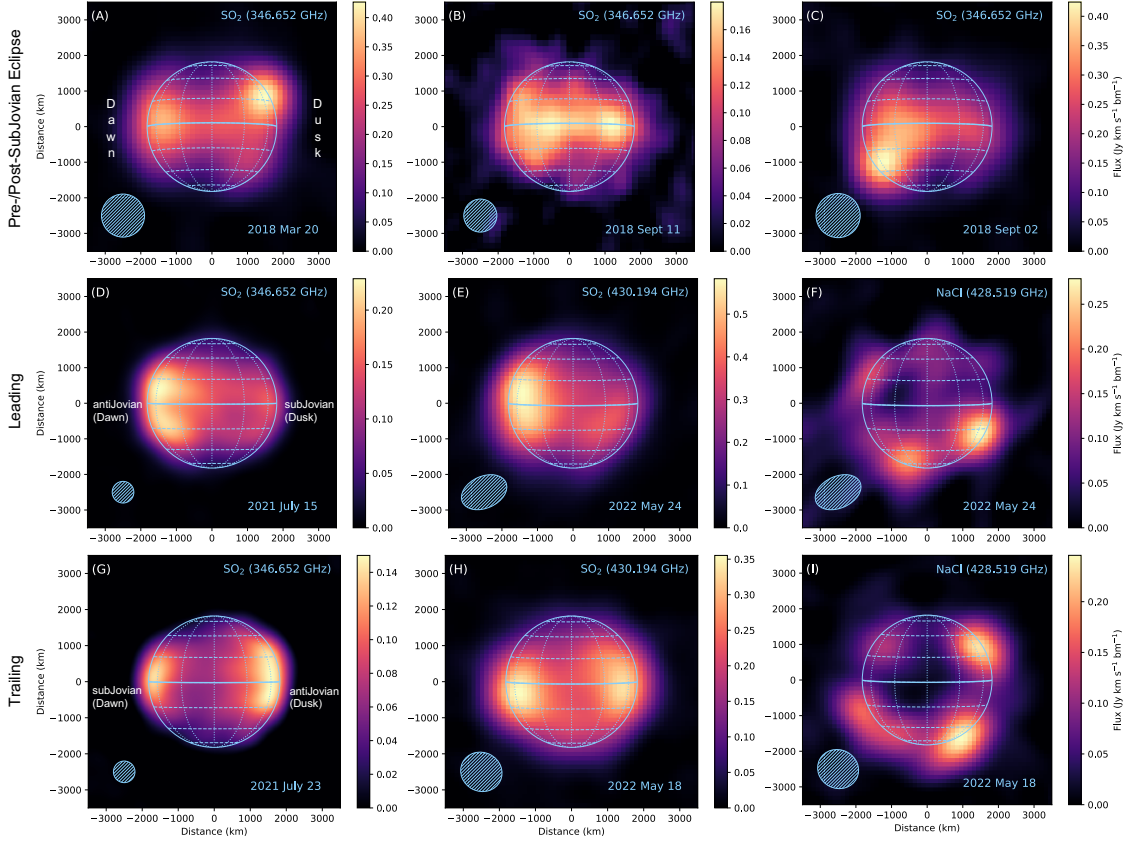


Figure 2. Integrated emission maps showing the distribution of Io’s SO_2 as observed before (A) and following (B, C) eclipse, at maximum east (D, E) and west (G, H) elongations. The NaCl distributions observed in 2022 are shown in panels F and I. Io’s dawn and dusk hemispheres, and the sub- and antiJovian directions (when relevant) are labeled for each row. Io’s latitude and longitude grid are shown in blue in 22.5° and 30° increments, respectively. The ALMA resolution element is shown in the bottom left as a hashed ellipse.

was then used to derive the spectral line center of each pixel, the frequency of which was compared to accurate rest frequency line centers from the Cologne Database for Molecular Spectroscopy (CDMS²; Müller et al., 2001, 2005; Endres et al., 2016) to derive the LOS velocity. Example fits for SO_2 and NaCl spectra are shown in Figure 3, where LOS velocities $> |250| \text{ m s}^{-1}$ were found; additional information is detailed in Appendix A.

For each observation, the LOS velocity fields derived from two or three spectral lines of SO_2 were combined into a weighted average. The different spectral transitions probe altitudes between $\sim 10\text{--}50 \text{ km}$ depending on the viewing geometry (de Pater et al., 2020; de Kleer et al., 2024); however, the derived velocities were fairly consistent across spectral transitions. Individual NaCl transitions are sensitive to altitudes below $\sim 30 \text{ km}$ (de Kleer et al., 2024). We leave the investigation of how the wind field varies as a function of altitude to future work, as it requires new observations with

² The CDMS can be accessed here: <https://cdms.astro.uni-koeln.de/>; see the SO_2 and NaCl entries and references therein.

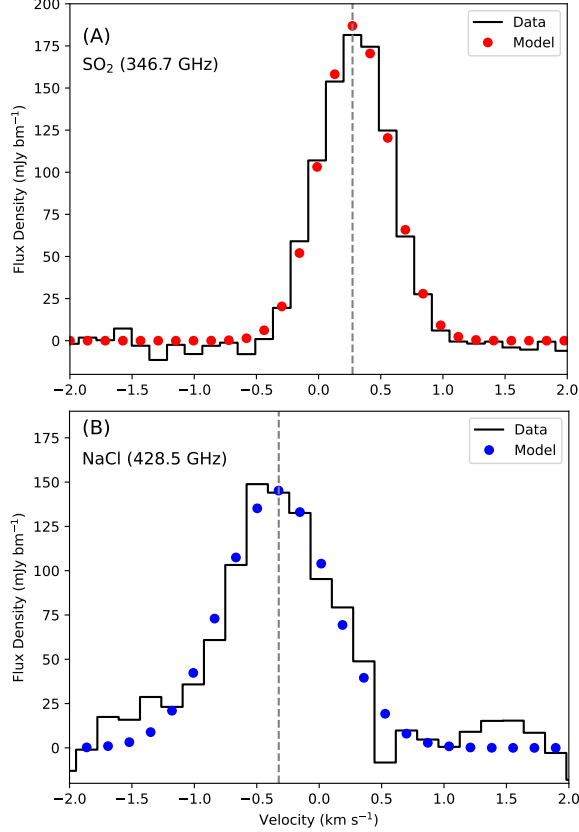


Figure 3. Spectra from individual pixels in ALMA images of Io (black) compared to best-fit model spectra (red, blue datapoints). The resulting LOS velocity fit is denoted by the dashed gray line. (A) SO₂ ($J_{K_a, K_c} = 19_{(1,19)} - 18_{(0,18)}$) transition at 346.7 GHz extracted from the equator on the dusk (antiJovian) limb of observations acquired on 2021 July 23 targeting Io’s trailing hemisphere (as shown in Figure 2G). The model fit results in a line-of-sight velocity of $259 \pm 11 \text{ m s}^{-1}$. (B) NaCl ($J = 33 - 32$) transition at 428.5 GHz extracted from the plume emission described by de Kleer et al. (2024) at $\sim 22^\circ\text{N}$, 159°W (their ‘location 3’) on 2022 May 24 (Figure 2F). A best-fit velocity of $-334 \pm 23 \text{ m s}^{-1}$ was found.

much higher spectral SNR over a smaller ALMA beam footprint, allowing for more accurate retrieval of winds on Io’s limb where the altitude differences may manifest more readily. The $1\text{-}\sigma$ velocity errors for each pixel were derived using a Monte Carlo method by fitting the derived Gaussian line shape from each spectrum to ~ 300 synthetic spectra as discussed in previous works (Lellouch et al., 2019; Cordiner et al., 2020). The wind errors ($\Delta\nu_{wind}$) can also be estimated based on the spectral SNR and full-width at half-maximum (FWHM) of the emission line (often $\sim 600 \text{ kHz}$ or $\sim 0.5 \text{ km s}^{-1}$; see de Pater et al., 2020; de Kleer et al., 2024), the central line frequency (ν_0 ; see Appendix A), the data channel width ($\Delta\nu$), and the speed of light (c) as discussed in Appendix D of Cavalié et al. (2021) using the empirical formula:

$$\Delta\nu_{wind} \sim \frac{FWHM}{SNR \times \sqrt{FWHM/\Delta\nu}} \times \frac{c}{\nu_0} \quad (1)$$

For the 2021 data, we find $\Delta\nu_{wind} \sim 8 \text{ m s}^{-1}$ using this formula for spectra with $\text{SNR} > 10$; these errors are commensurate with the errors derived through the Monte Carlo analysis. To assist in interpretation of the derived velocity and wind maps, pixels with distances away from Io’s surface greater than the ALMA beam half-width ($\sim 600\text{--}1200 \text{ km}$) were masked out, as well as pixels with spectra $\text{SNR} < 10$. The errors associated with these pixels are often $\gtrsim 25 \text{ m s}^{-1}$, approaching the magnitude of velocity values found on the disk. The weighted average LOS velocity maps and the associated maps of velocity uncertainty are shown and discussed in Appendix A.

Finally, Io’s solid-body rotation at every latitude and longitude was calculated and subtracted from the LOS velocity field. The solid-body rotation model was convolved with the appropriate ALMA beam size and shape before subtraction to account for smearing of the velocities across the beam. A comparison of the data and rotation models is shown in Appendix B. With the solid-body rotation subtracted, the derived velocities now represent the LOS winds as observed at each pixel location.

4. RESULTS & DISCUSSION

The full set of derived wind maps is shown in Figure 4 following the subtraction of Io’s solid-body rotation, with positive (red) pixels representing winds moving away from the observer, and negative (blue) pixels for winds moving towards. For reference, the median $3\text{-}\sigma$ velocity errors are denoted on the colorbar for each map (black lines), allowing for the assessment of the significance of the wind field in each location; the full error maps are shown in Appendix A. It should also be noted that though the atmosphere may experience (potentially strong) winds at all latitudes and longitudes, the spatial distribution and SNR of the SO_2 and NaCl lines measured in these observations constrained our ability to measure the wind field at all locations (see Figure 2). Additionally, the Doppler winds were derived from radial velocities and thus only represent the LOS component.

4.1. *Eclipse Observations*

Figure 4A–C shows the distribution of SO_2 winds from Io’s ingress into (panel A) and egress from (panels B, C) eclipse by Jupiter. While the observations were originally designed to measure the distribution of SO_2 pre- and post-eclipse on the subJovian hemisphere, they were utilized here to place constraints on two aspects of the wind field: how long the wind field takes to manifest after Io experiences daylight following eclipse, and to what degree pressure from the plasma torus impacts the measured SO_2 winds, since they provide measurements of Io when the local plasma velocity has no LOS component.

Figure 4A shows the distribution of SO_2 winds on Io’s subJovian hemisphere ~ 30 min before entering eclipse on 2018 March 20. Here, we find receding winds at most longitudes on Io’s dawn hemisphere, reaching speeds $> 100 \text{ m s}^{-1}$ towards the equatorial limb. Winds approaching the observer are detected towards the dusk limb at reduced magnitudes, though at the $\sim 3\text{-}\sigma$ level. The impact of the plasma

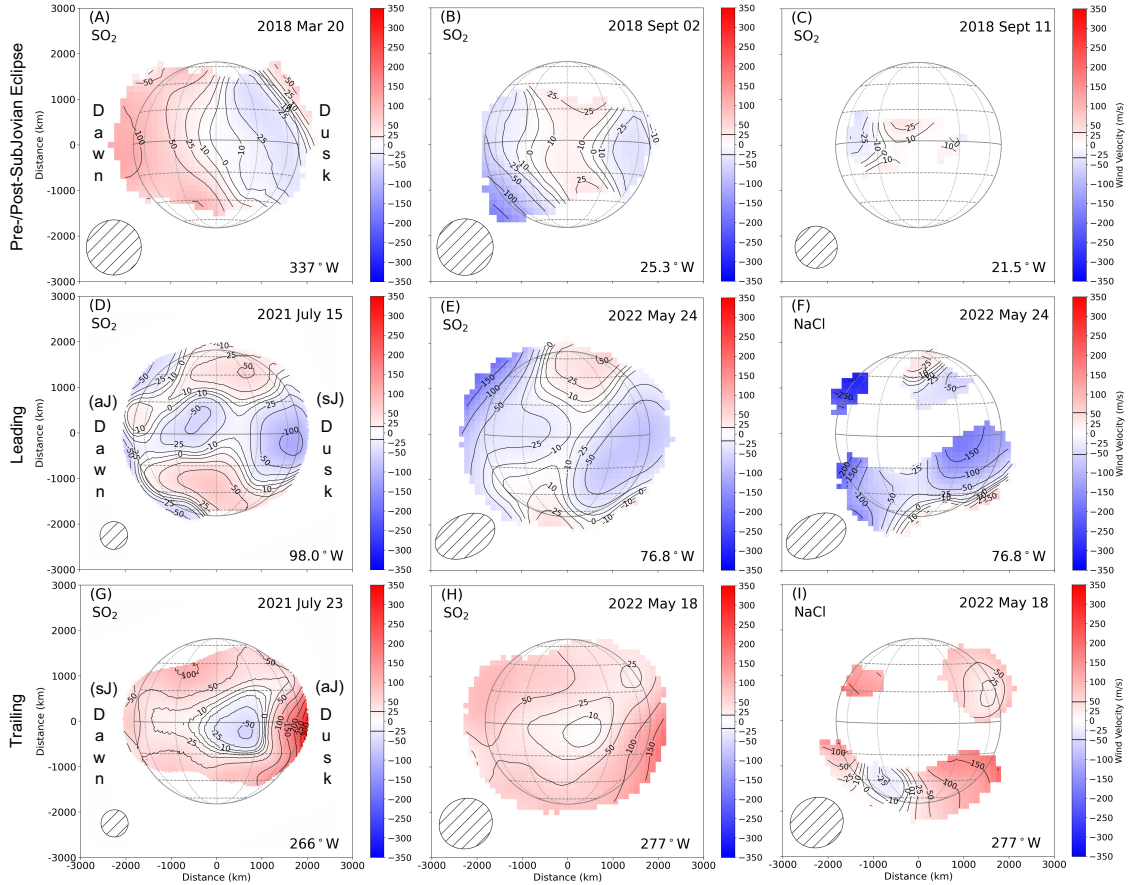


Figure 4. Derived line-of-sight wind maps following the Doppler shift fitting of Io’s velocity field and the subtraction of Io’s solid-body rotation. Only pixels with spectral SNR ≥ 10 are shown. Blue velocities correspond to winds approaching the observer, while red velocities are receding. The corresponding velocity maps and uncertainties are shown in Appendix A. Wind maps are grouped loosely by observation and longitude. Observational parameters are detailed in Table 1. Panels A–C show SO₂ winds on the subJovian hemisphere as Io entered (A) and exited (B, C) eclipse in 2018; panels D and G show SO₂ winds at Jupiter’s eastern and western elongation, respectively, from 2021; panels E, F, H, and I show SO₂ and NaCl winds at both Jovian elongations from 2022. Io’s dawn and dusk hemispheres are labeled in each row, as are the sub- and antiJovian directions (sJ and aJ, respectively). Io’s solid-body radius, latitude and longitude lines are shown as a gray grid – latitude and longitude contours increase in increments of 22.5° and 30°, respectively. The central sub-observer longitude is denoted in the lower right of each panel. The corresponding ALMA beam (FWHM of the PSF) for each observation is shown as a hashed ellipse in the bottom left of each panel. The median 3- σ wind errors are shown as solid lines on the color bar for each panel for reference; see Appendix A for the full uncertainty maps.

torus on Io’s wind field is predicted to be complex (Walker, 2012), but viewing Io’s subJovian hemisphere removes the majority of the perpendicular wind component due to the torus flow; as such, Figure 4A can be used as a proxy for the underlying wind field before Io goes into eclipse, which may be indicative of the subJovian winds caused mainly by sublimation-driven gradients (see Figure 1A). Indeed, the wind field predicted by models using the SO₂ frost and temperature distributions on Io (Gratiy et al., 2010; Walker et al., 2012) show winds moving in day-to-night streams from

equatorial latitudes (seen as receding winds in our LOS observations) and lagging $\sim 30^\circ$ east of the sub-solar longitude, where the peak surface frost temperatures result in slower (~ -10 – 100 m s^{-1}) winds approaching the observer, similar to what we measure here.

Winds from an observation ~ 30 minutes following eclipse is shown in Figure 4B from 2018 September 02. Here, we measure approaching winds at Io’s dawn limb reaching maximum speeds around -100 m s^{-1} . Winds at the dusk limb are also approaching, though at a reduced speed, and winds up to $\sim 25 \text{ m s}^{-1}$ (at the $3\text{-}\sigma$ level) are receding at the central longitude. Figure 4C shows the wind field from a second observation following eclipse, which started just after (~ 7 min) Io’s egress from behind Jupiter’s shadow on 2018 September 11. As shown in [de Pater et al. \(2020\)](#), the emission of SO_2 at this time was faint, and confined to low latitudes. The wind field we measure here is statistically insignificant (i.e., the winds are $<3\text{-}\sigma$) in all pixels. The comparison of the SO_2 distributions in Figure 2B and C shows that the SO_2 atmosphere has rebuilt in <30 min following eclipse ([de Pater et al., 2020](#)); similarly, the wind fields in Figure 4B and C shows the rapid build up of winds during this period. The sublimation-driven winds were predicted to be weak for ~ 1 hr following egress from eclipse and may originate $\sim 10^\circ\text{E}$ of the subsolar point by [Walker et al. \(2012\)](#), which may explain the low-magnitude receding winds observed in Figure 4B. The higher magnitude approaching winds along the dawn hemisphere may be due to the emerging dawn atmospheric enhancement, which takes ~ 40 min to establish following eclipse ([Walker et al., 2012](#)), and may dominate the sublimation-driven winds at this point following eclipse.

4.2. *Leading Hemisphere Winds*

The maps in Figure 4D–F show the SO_2 and NaCl winds measured on Io’s leading hemisphere ($\sim 90^\circ\text{W}$ longitude, at maximum eastern Jovian elongation) during 2021 and 2022. At this point in its orbit, Io has experienced significantly more daylight than the post-eclipse observations (Figure 4B and C), so the SO_2 emission (Figure 2D, E) was strong enough to measure the winds at most latitudes and with smaller errors. Though the SO_2 observations (Figure 4D, E) are temporally separated and are at different spatial resolutions (denoted by the ALMA beam in the lower left of each panel), the wind distributions are largely consistent. We observe approaching winds at speeds ranging from roughly -10 to -100 m s^{-1} along the equator and towards the limbs, with receding winds up to 50 m s^{-1} towards higher latitudes, which are greater in magnitude than those tentatively measured post-eclipse in Figure 4B. These receding winds are again likely tracers of the day-to-night flow driven by equatorial sublimation-driven pressure gradients, while the sublimation itself may manifest as winds in the approaching direction along the equator (Figure 1A). The wind field we observe on the leading hemisphere is inconsistent with that measured by [Moulet et al. \(2008\)](#) with the IRAM/PdBI, where receding winds up to $\sim 150 \text{ m s}^{-1}$ were

observed on the dusk hemisphere. A significant difference ($\sim |100 - 150| \text{ m s}^{-1}$) in the wind flow is required to reconcile the winds measured between the ALMA and PdBI observations on the leading hemisphere dusk limb, as the wind field we find in both observations does not resemble a prograde flow.

The Jovian plasma torus is impacting the opposite hemisphere to those observed in Figure 4D–F, and thus may reinforce the approaching wind flow as it wraps around the moon and transfers momentum to the atmosphere (see Figure 1B). In the SO_2 wind field, the approaching winds are not significantly increased in magnitude compared to the observations of Io following eclipse egress (Figure 4B), where the toroidal motion was roughly perpendicular to the line of sight. Increased winds at the dusk limb (particularly in Figure 4D) may be evidence of torus momentum transfer, as the winds are predicted to be largely receding towards the dusk terminator (Graty et al., 2010; Walker et al., 2012; Walker, 2012); receding winds on the dusk hemisphere were also observed by Moullet et al. (2008). The winds measured using NaCl emission (Figure 4F) present additional evidence for the large influence of upstream torus pressure. We measure only approaching NaCl winds (i.e., in the direction of Io’s orbit and the rotation of the plasma torus), reaching velocities up to -300 m s^{-1} . No evidence of the day-to-night, sublimation-driven flow is observed in the NaCl wind field due to the lack of measurable receding winds; however, this may also be the result of the localized nature of the NaCl emission.

4.3. *Trailing Hemisphere Winds*

The winds measured from SO_2 and NaCl emission lines on Io’s trailing hemisphere ($\sim 270^\circ\text{W}$ longitude, western Jovian elongation) in 2021 and 2022 are shown in Figure 4G–I. The trailing hemisphere winds are significantly different from those observed on the leading hemisphere. Here, we observe primarily receding winds, which reach velocities $>200 \text{ m s}^{-1}$ away from the observer at Io’s dusk limb. At the higher resolution observation (Figure 4G), we also measure winds approaching the observer at speeds reaching roughly -50 m s^{-1} localized along the equator. This observation represents the best comparison to models of the Ionian wind field, which predict winds emanating from along the equator lagging the sub-solar longitude and receding winds at other latitudes and longitudes following the day-to-night streams (Figure 1A). The flow at the dawn limb is counteracted by Io’s rotation and potentially through the SO_2 DAE predicted by Walker et al. (2010), which would deplete (and possibly collapse) the westward flow towards the terminator. While the DAE in SO_2 emission has yet to be definitively observed (de Pater et al., 2023a), an enhancement of SO_2 is apparent on the subJovian hemisphere in our trailing hemisphere observations from 2021 and 2022 (Figure 2G and H, respectively). A pressure differential between the high column density SO_2 region on the limb and longitudes just experiencing sunlight to the west may interfere with the sublimation-driven flow (Walker et al., 2012). We do not observe the approaching wind feature near the sub-observer longitude in

Figure 4H, though the relatively larger ALMA resolution here may smear the localized approaching winds across the beam shape, resulting in decreased receding winds at similar longitudes along the equator. Slight differences in SO_2 frost distribution, or temporal variability in volcanic activity, could also decrease the approaching winds measured between the two observations.

As the toroidal momentum experienced by Io's trailing hemisphere would reinforce receding winds (i.e., the sub-solar and sub-plasma points are approximately equal here), the increased speeds at Io's dusk limb compared to those post-eclipse (Figure 4A) may be indicators of this effect (see the diagram in Figure 1C); compared to the dusk limb of the pre-eclipse observation, the winds measured at maximum western elongation are significantly ($\sim 200 \text{ m s}^{-1}$) higher. On the contrary, the dawn winds exhibited by the observations on the trailing hemisphere are somewhat diminished compared to the pre-eclipse elongation ($\sim 50 \text{ m s}^{-1}$ and $\sim 100 \text{ m s}^{-1}$, respectively) which confounds this picture. Invoking the DAE would help to explain the discrepancy between the dawn and dusk limbs, as both would experience momentum from the plasma torus but only winds on the dawn terminator would be disrupted by counter (approaching) flow from the DAE. The consistent $50\text{--}200 \text{ m s}^{-1}$ winds we observe in the trailing hemisphere NaCl map (Figure 4I) lends credence to the notion that the NaCl winds are primarily driven by torus interactions, as on the leading hemisphere (Figure 4F) – at the viewing geometry of this observation, NaCl LOS velocities driven purely by volcanic activity seems unlikely.

5. CONCLUSIONS: AN EMERGING PICTURE OF IO'S WIND FIELD

Through the analysis of LOS Doppler-shift maps from multiple ALMA observations of Io, we have found striking differences in Io's wind distributions as a function of longitude and differences in wind speed magnitude with molecular species. Unlike previous observations of the prograde, super-rotating wind field by Moullet et al. (2008), the winds we measure here do not resemble those found on other planetary bodies measured thus far, likely due to the combination of low atmospheric pressures, volcanic and plasma phenomena present on Io that impact the atmospheric flow. By assessing the maps from SO_2 and NaCl at different viewing geometries, we can draw some broad conclusions. Winds in the bulk SO_2 atmosphere within $\sim 30^\circ$ of the subsolar point are receding at $\sim 25\text{--}50 \text{ m s}^{-1}$ on both hemispheres, driven by day-to-night pressure and temperature gradients. Localized approaching winds are detected in variable locations along the equator, and can be explained by SO_2 frost sublimation from a heterogeneous SO_2 frost distribution. Finally, the largest magnitude winds we observe in SO_2 at each maximum elongation are in the direction of Io's orbital motion, and also the direction of the rapid plasma torus rotation, which overtakes Io at a relative velocity of 57 km s^{-1} . This, combined with the NaCl wind maps that only show motion in the orbital direction, is evidence that torus interactions – such as momentum transfer – alter the SO_2 wind field, and may be the major drivers of

the NaCl winds. However, the complex SO₂ wind fields and the number of processes contributing to the SO₂ winds make it difficult to determine the relative contribution of torus pressure compared to other proposed mechanisms.

It is clear that Io's wind field at low altitudes ($\lesssim 50$ km) is influenced by both external (the Jovian plasma torus) and Iogenic (frost sublimation, volcanic plume) activity, and is both locally and temporally variable. Further, our ability to probe the winds depends on the availability of strong atmospheric rotational line emission, which can be asymmetrically distributed across Io. In the future, it will be important to analyze the wind field derived from multiple atmospheric species at multiple times during Io's orbit, and potentially at multiple times throughout its year. Further observations at higher angular resolution, across multiple sub-observer longitudes and atmospheric species, would help to elucidate the connection between these processes in a more systematic way. If taken concurrent with observations that trace volcanic thermal emission, future measurements could reinforce the somewhat tenuous connections we observe here in the processes on the surface and in the Jovian environment that drive Io's complex meteorology.

6. ACKNOWLEDGMENTS

Funding for this work was provided by the NASA ROSES Solar System Observations program for A.E.T. and M.A.C. K.d.K. acknowledges support from the National Science Foundation (NSF) under Grant #2238344 through the Faculty Early Career Development Program. I.d.P. and S.L-C. acknowledge funding from NASA Solar System Workings Grant #80NSSC24K0306, as a subawardee of the lead campus, University of Texas at Austin.

This paper makes use of the following ALMA data: ADS/JAO.ALMA#2017.1.00670.S, 2019.1.00216.S, and 2021.1.00849.S. ALMA is a partnership of ESO (representing its member states), NSF (USA) and NINS (Japan), together with NRC (Canada), MOST and ASIAA (Taiwan), and KASI (Republic of Korea), in cooperation with the Republic of Chile. The Joint ALMA Observatory is operated by ESO, AUI/NRAO and NAOJ. The National Radio Astronomy Observatory is a facility of the National Science Foundation operated under cooperative agreement by Associated Universities, Inc.

A. VELOCITY FITTING AND MAPS

An example of spectral Doppler shifts exhibited by the Io data are shown in Figure 5, which displays averaged SO₂ spectra extracted from 10×10 pixel areas originating from the location of each box with respect to Io's surface (gray grid in the background). For averaged spectra with sufficient SNR, the location of the SO₂ line center can be indicative of the Doppler shift produced through the radial velocity induced by Io's rotation and wind field in the approaching (blue-shift) or receding (red-shift) directions. The derivation of Io's winds is made more accurate by fitting the spectrum from each pixel with a Gaussian function, as described in Section 3.

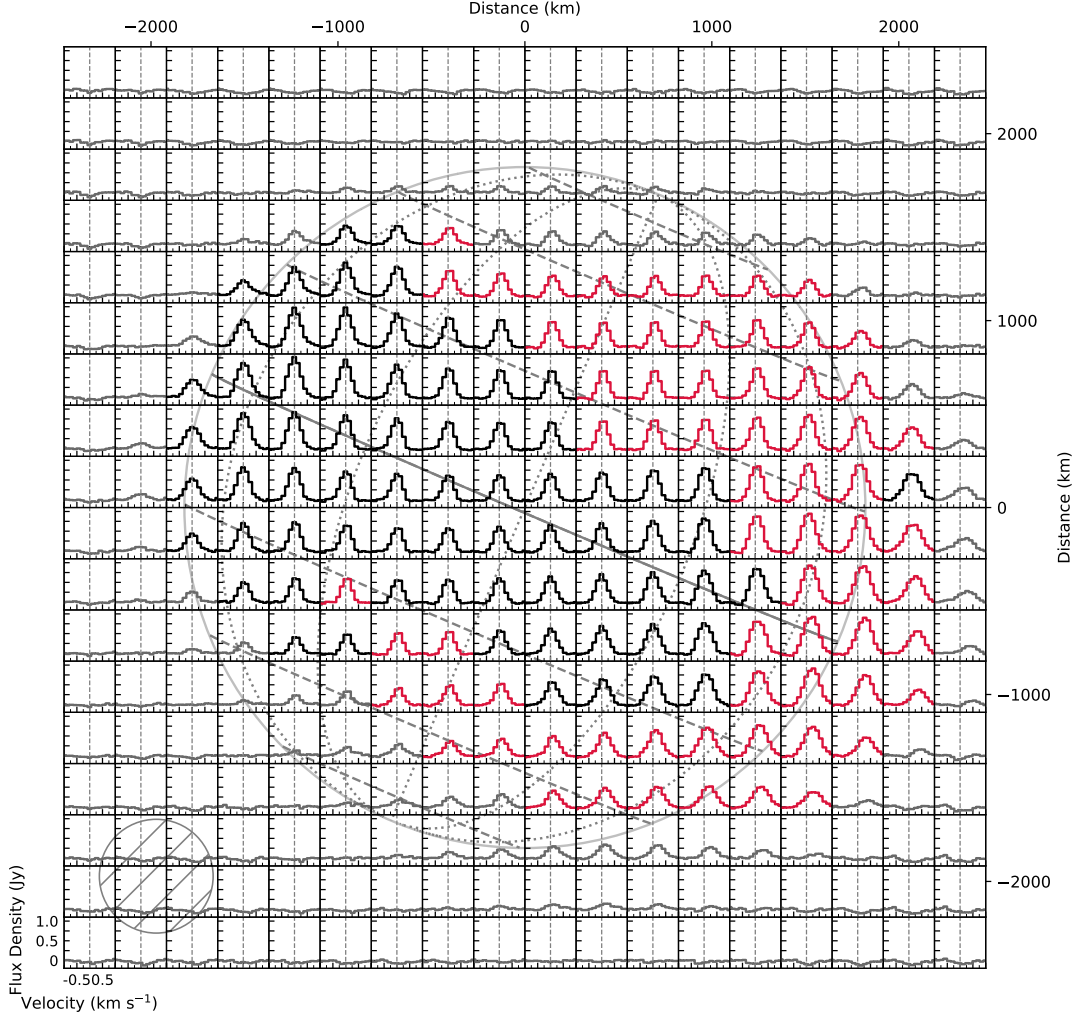


Figure 5. Grid of continuum-subtracted SO_2 ($J_{K_a, K_c} = 19_{(1,19)} - 18_{(0,18)}$) spectra from observations of Io’s trailing hemisphere from 2021 July 23. Spectra are presented in units of velocity; vertical dashed grey lines indicate the rest frequency of the line (zero velocity shift). The spectrum in each panel corresponds to the average of 100 pixels contained within each 10×10 pixel region. The flux density and velocity scales are shown on the lower left panel. Spectra with $\text{SNR} < 10$ are shown in gray, and those with $\text{SNR} \geq 10$ are shown in black. To demonstrate the observed Doppler shifts, spectra are colored red where the frequency of the maximum channel falls to the right of the SO_2 rest frequency by $>1/2$ of a spectral channel (61 kHz; $\sim 60 \text{ m s}^{-1}$). Io’s solid-body radius is shown, as are latitude and longitude lines at 22.5° and 30° increments, respectively, in gray. Note that the north pole of Io is not rotated to align with the y-axis. The ALMA resolution element is shown as the gray hashed ellipse in the bottom left, which smears emission off of Io’s disk.

The retrieved central frequencies are then compared to those found by laboratory measurements and previous observations, such as those documented on the CDMS; the full spectral line parameters for the SO_2 and NaCl transitions analyzed here are listed in Table 2.

Figure 6 shows the derived LOS velocities for the combined SO_2 spectral line measurements (panels A–E, G, H) and NaCl ($J = 33 - 32$) spectral line (panels F, I).

Table 2. Observed Spectral Transitions

Project Code #	Species	Transition ^a (J_{K_a, K_c})	Rest Freq. ^b (MHz)	E_u (K)
2017.1.00670.S	SO ₂	16 _(4,12) – 16 _(3,13)	346523.8784	164.5
	SO ₂	19 _(1,19) – 18 _(0,18)	346652.1691	168.1
2019.1.00216.S	SO ₂	19 _(1,19) – 18 _(0,18)	346652.1691	168.1
	SO ₂	20 _(0,20) – 19 _(1,19)	358215.6327	185.3
2021.1.00849.S	SO ₂	28 _(5,23) – 28 _(4,24)	416825.5576	435.9
	SO ₂	31 _(4,28) – 31 _(3,29)	419019.0378	497.0
	SO ₂	24 _(1,23) – 23 _(2,22)	430193.7070	280.5
	NaCl	33 – 32	428518.5512	350.1

NOTE—^aSpectral transitions are written from the rotational upper (J_u) to lower (J_l) energy states with the projections onto the A and C inertial axes as K_a and K_c , respectively. ^bRest frequencies are extracted from the CDMS entries for SO₂ and NaCl from the references therein.

The associated errors, as derived from Monte Carlo estimation, are shown in Figure 7. Following the removal of Io’s solid-body rotation (Appendix B), these radial velocity maps were used to produce the final wind speeds shown in Figure 4 in Section 4.

These maps show SO₂ LOS radial velocities that vary spatially and fluctuate between $\sim |50|$ m s⁻¹ on the disk, reaching maximum values of 200–300 m s⁻¹ towards the limbs, with typical errors on order 5–10 m s⁻¹. The velocity uncertainties increase to ~ 15 –20 m s⁻¹ as the spectral SNR degrades, typically at high latitudes and off disk where the atmosphere is increasingly rarefied as found by previous observations (de Pater et al., 2021, 2023a). The NaCl velocities consistently reach $> |100|$ m s⁻¹, up to $\sim |350|$ m s⁻¹, though with larger associated errors (~ 15 –30 m s⁻¹). The NaCl emission is confined to localized, high column density regions attributed to volcanic outgassing (Redwing et al., 2022; de Kleer et al., 2024), with considerable uncertainty elsewhere. As such, the spatial distribution of both SO₂ and NaCl constrains the sampling of the atmospheric wind field, in addition to the aforementioned spectral SNR. While regions of low column density can still experience high wind velocities (see Walker et al., 2012; Walker, 2012), these regions primarily occur on the terminators or nightside, or are difficult to sound with spectroscopic techniques.

B. SUBTRACTION OF THE UNDERLYING SOLID-BODY ROTATION

The radial velocity measurements presented in Appendix A contain a superposition of Io’s innate solid-body rotation and any additional atmospheric motion – related to sublimation-driven winds, toroidal momentum transfer, volcanic outgassing, or otherwise. Io’s solid-body angular velocity (Ω) is $|75|$ m s⁻¹, which is significant

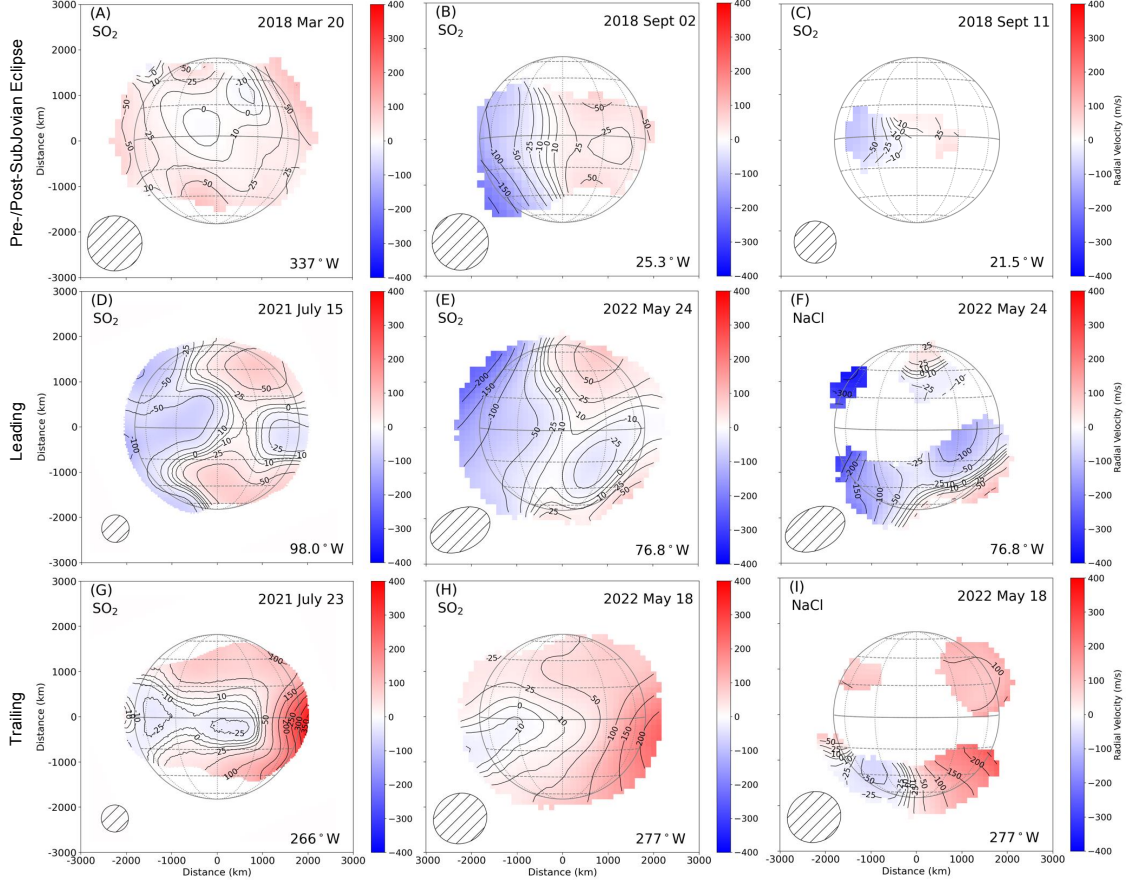


Figure 6. Retrieved SO_2 and NaCl LOS velocity maps for pixels with spectral $\text{SNR} \geq 10$ used to derive Io's wind field shown in Figure 4. The colorbar corresponds to approaching (blue) and receding (red) LOS velocities. SO_2 velocities on Io's subJovian hemisphere pre- and post-eclipse from observations in 2018 are shown in panels A–C; SO_2 velocities at Jupiter's eastern and western elongations are shown in panels D and G for observations in 2021, E and H for observations in 2022; NaCl velocities from both Jovian elongations observed in 2022 are shown in panels F and I. Each panel corresponds to those in Figure 4 before the subtraction of Io's solid-body rotation. Io's solid-body radius, latitude and longitude lines are denoted by the gray grid, with latitude and longitude contours increasing in increments of 22.5° and 30° , respectively. The sub-observer central longitude is shown in the lower right of each panel, and the ALMA beam (FWHM of the PSF) for each observation is shown as a hashed ellipse in the lower left of each panel.

enough to impact the gas velocities predicted through models (Gratiy et al., 2010; Walker et al., 2012); this motion may counteract (and reverse) sublimation-driven flow on the dawn terminator, while reinforcing it on the dusk terminator. To remove this effect and isolate velocities due to winds (and their underlying drivers), we calculated the latitude (θ) and longitude (ϕ) of every x, y pixel pair in each ALMA image and determined the modeled solid-body velocity, $V_m(x, y)$, through the relation with the angular velocity:

$$V_m(x, y) = \Omega \cos\theta(x, y) \sin(\phi(x, y) - \phi_{obs}) \cos\theta_{obs} \quad (2)$$

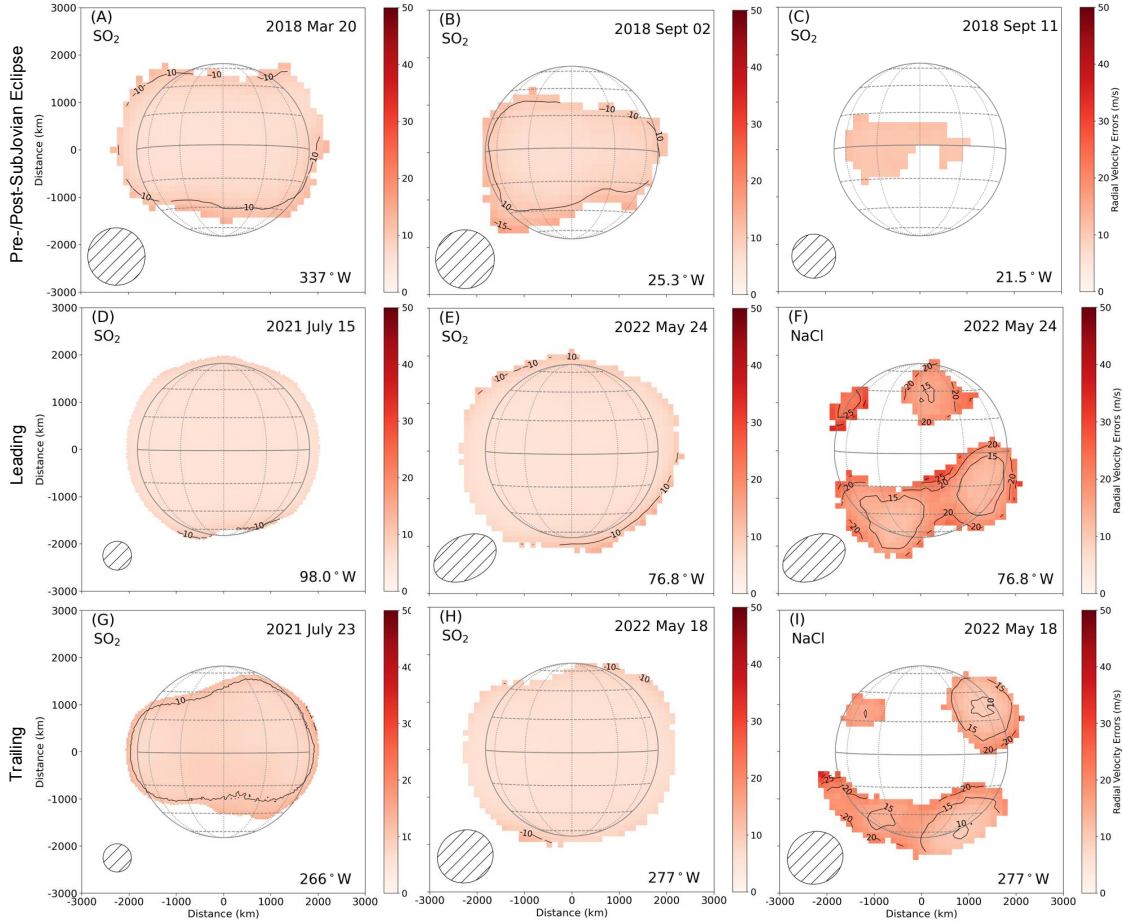


Figure 7. Retrieved velocity error maps corresponding to the velocity maps shown in Figure 6. Velocity errors are shown where the gas emission is $\geq 10\times$ the spectral RMS noise and within an ALMA beam-width (shown in the lower left) of Io’s surface. Io’s solid-body radius, latitude (22.5° increments) and longitude (30° increments) lines are represented by the grid in gray.

where θ_{obs} and ϕ_{obs} correspond to the sub-observer latitude and longitude, respectively, of each observation (see Table 1).

Figure 8 shows an example of a single retrieved SO_2 velocity field (panel A) compared to the model of Io’s solid-body rotation as a function of latitude and longitude (panel B). Without further modification, the wind field produced by subtracting the solid-body model from the measured velocity field is shown in Figure 8E. However, the smearing of SO_2 emission across the ALMA beam shape must also be accounted for; the discontinuous winds exhibited at the limbs in Figure 8E are caused by subtracting the pure solid-body velocity from the retrieved velocities, which are innately convolved by the ALMA beam. Figure 8C shows the solid-body model (panel B) convolved with the ALMA beam, a 2D Gaussian function. While the resulting winds (Figure 8F) present smoother gradients at the limbs, the limb velocities themselves are not properly accounted for due to the convolution of the ALMA beam shape with surrounding space at 0 m s^{-1} . This is corrected in Figure 8D, where the solid-body

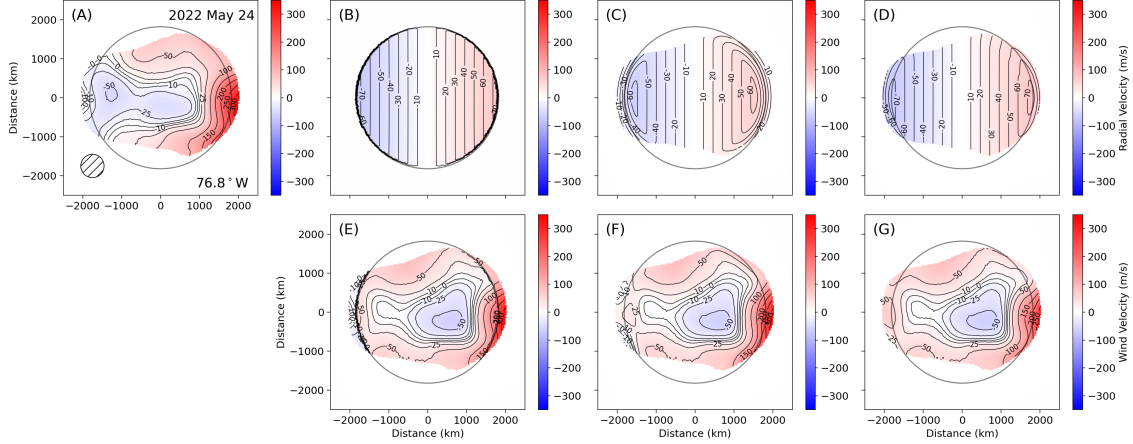


Figure 8. Comparison of the retrieved wind map of the SO_2 ($J_{K_a, K_c} = 19_{1,19} - 18_{0,18}$) spectral line at 346.7 GHz (A) with solid-body rotation models (B–D) and the final, derived wind maps (E–G) following the subtraction of the models from the data. Different rotation models were tested: a pure solid-body rotation model (B); the solid-body rotation model convolved with the ALMA beam (C); solid-body rotation extending off the surface of Io to the ALMA beam width, and subsequently convolved with the beam shape (D). The wind fields (E–G) result from the velocity field (A) subtracted by the corresponding model in the panel above (e.g., velocities A - model B = winds E).

rotation is projected beyond Io’s radius by an ALMA beam width or to the point at which the spectral $\text{SNR} \leq 10$, and subsequently convolved with the beam shape. Though a somewhat coarse approximation, the connection between the motion of each atmospheric species and the surface – before invoking atmospheric winds – is difficult to assume based on the generation of SO_2 or NaCl through sublimation, sputtering, or outgassing, which each may produce gas with a natural velocity dispersion that is disconnected with the solid-body. However, the model sufficiently removes edge effects produced through the subtraction of the solid-body model (Figure 8B) alone, and the differences due to the extension of the model into the atmosphere are not significant compared to the noise towards the limb (compare the limb velocities in Figure 8F and G). A more rigorous consideration of these effects, and the inclusion of an additional component simulating the torus momentum transfer, should be incorporated into future work.

REFERENCES

- Achterberg, R. K., Conrath, B. J., Gierasch, P. J., Flasar, F. M., & Nixon, C. A. 2008, *Icarus*, 194, 263, doi: [10.1016/j.icarus.2007.09.029](https://doi.org/10.1016/j.icarus.2007.09.029)
- Austin, J. V., & Goldstein, D. B. 2000, *Icarus*, 148, 370, doi: [10.1006/icar.2000.6466](https://doi.org/10.1006/icar.2000.6466)
- Bagenal, F., & Dols, V. 2023, in *Astrophysics and Space Science Library*, Vol. 468, Io: A New View of Jupiter's Moon, ed. R. M. C. Lopes, K. de Kleer, & J. T. Keane, 291–322, doi: [10.1007/978-3-031-25670-7_9](https://doi.org/10.1007/978-3-031-25670-7_9)
- Benmahi, B., Cavalié, T., Fouchet, T., et al. 2022, *A&A*, 666, A117, doi: [10.1051/0004-6361/202244200](https://doi.org/10.1051/0004-6361/202244200)
- Briggs, D. S. 1995, PhD thesis, New Mexico Institute of Mining and Technology
- Carrión-González, Ó., Moreno, R., Lellouch, E., et al. 2023, *A&A*, 674, L3, doi: [10.1051/0004-6361/202346621](https://doi.org/10.1051/0004-6361/202346621)
- CASA Team, Bean, B., Bhatnagar, S., et al. 2022, *PASP*, 134, 114501, doi: [10.1088/1538-3873/ac9642](https://doi.org/10.1088/1538-3873/ac9642)
- Cavalié, T., Benmahi, B., Hue, V., et al. 2021, *A&A*, 647, L8, doi: [10.1051/0004-6361/202140330](https://doi.org/10.1051/0004-6361/202140330)
- Cordiner, M. A., Garcia-Berrios, E., Cosentino, R. G., et al. 2020, *ApJL*, 904, L12, doi: [10.3847/2041-8213/abc688](https://doi.org/10.3847/2041-8213/abc688)
- de Kleer, K., Hughes, E. C., Nimmo, F., et al. 2024, *Science*, 384, 682, doi: [10.1126/science.adj0625](https://doi.org/10.1126/science.adj0625)
- de Kleer, K., de Pater, I., Molter, E. M., et al. 2019, *AJ*, 158, 29, doi: [10.3847/1538-3881/ab2380](https://doi.org/10.3847/1538-3881/ab2380)
- de Pater, I., Goldstein, D., & Lellouch, E. 2023a, in *Astrophysics and Space Science Library*, Vol. 468, Io: A New View of Jupiter's Moon, ed. R. M. C. Lopes, K. de Kleer, & J. T. Keane, 233–290, doi: [10.1007/978-3-031-25670-7_8](https://doi.org/10.1007/978-3-031-25670-7_8)
- de Pater, I., Keane, J. T., de Kleer, K., & Davies, A. G. 2021, *Annual Review of Earth and Planetary Sciences*, 49, doi: [10.1146/annurev-earth-082420-095244](https://doi.org/10.1146/annurev-earth-082420-095244)
- de Pater, I., Luszcz-Cook, S., Rojo, P., et al. 2020, *PSJ*, 1, 60, doi: [10.3847/PSJ/abb93d](https://doi.org/10.3847/PSJ/abb93d)
- de Pater, I., Lellouch, E., Strobel, D. F., et al. 2023b, *Journal of Geophysical Research (Planets)*, 128, e2023JE007872, doi: [10.1029/2023JE007872](https://doi.org/10.1029/2023JE007872)
- Endres, C. P., Schlemmer, S., Schilke, P., Stutzki, J., & Müller, H. S. P. 2016, *Journal of Molecular Spectroscopy*, 327, 95, doi: [10.1016/j.jms.2016.03.005](https://doi.org/10.1016/j.jms.2016.03.005)
- Feaga, L. M., McGrath, M., & Feldman, P. D. 2009, *Icarus*, 201, 570, doi: [10.1016/j.icarus.2009.01.029](https://doi.org/10.1016/j.icarus.2009.01.029)
- Flasar, F. M., Achterberg, R. K., Conrath, B. J., et al. 2005, *Science*, 307, 1247, doi: [10.1126/science.1105806](https://doi.org/10.1126/science.1105806)
- Giles, R. S., Spencer, J. R., Tsang, C. C., et al. 2024, *Icarus*, 418, 116151, doi: [10.1016/j.icarus.2024.116151](https://doi.org/10.1016/j.icarus.2024.116151)
- Giono, G., & Roth, L. 2021, *Icarus*, 359, 114212, doi: [10.1016/j.icarus.2020.114212](https://doi.org/10.1016/j.icarus.2020.114212)
- Gratiy, S. L., Walker, A. C., Levin, D. A., et al. 2010, *Icarus*, 207, 394, doi: [10.1016/j.icarus.2009.11.004](https://doi.org/10.1016/j.icarus.2009.11.004)
- Hanel, R., Conrath, B., Flasar, M., et al. 1979, *Science*, 204, 972, doi: [10.1126/science.204.4396.972](https://doi.org/10.1126/science.204.4396.972)
- Högbom, J. A. 1974, *A&AS*, 15, 417
- Ingersoll, A. P. 1989, *Icarus*, 81, 298, doi: [10.1016/0019-1035\(89\)90055-9](https://doi.org/10.1016/0019-1035(89)90055-9)
- Ingersoll, A. P., Summers, M. E., & Schlipf, S. G. 1985, *Icarus*, 64, 375, doi: [10.1016/0019-1035\(85\)90062-4](https://doi.org/10.1016/0019-1035(85)90062-4)
- Jessup, K. L., & Spencer, J. R. 2015, *Icarus*, 248, 165, doi: [10.1016/j.icarus.2014.10.020](https://doi.org/10.1016/j.icarus.2014.10.020)
- Jessup, K. L., Spencer, J. R., Ballester, G. E., et al. 2004, *Icarus*, 169, 197, doi: [10.1016/j.icarus.2003.11.015](https://doi.org/10.1016/j.icarus.2003.11.015)

- Kliore, A., Cain, D. L., Fjeldbo, G., Seidel, B. L., & Rasool, S. I. 1974, *Science*, 183, 323, doi: [10.1126/science.183.4122.323](https://doi.org/10.1126/science.183.4122.323)
- Lellouch, E., Ali-Dib, M., Jessup, K. L., et al. 2015, *Icarus*, 253, 99, doi: [10.1016/j.icarus.2015.02.018](https://doi.org/10.1016/j.icarus.2015.02.018)
- Lellouch, E., Belton, M., de Pater, I., Gulkis, S., & Encrenaz, T. 1990, *Nature*, 346, 639, doi: [10.1038/346639a0](https://doi.org/10.1038/346639a0)
- Lellouch, E., Belton, M., de Pater, I., et al. 1992, *Icarus*, 98, 271, doi: [10.1016/0019-1035\(92\)90095-O](https://doi.org/10.1016/0019-1035(92)90095-O)
- Lellouch, E., Paubert, G., Moses, J. I., Schneider, N. M., & Strobel, D. F. 2003, *Nature*, 421, 45, doi: [10.1038/nature01292](https://doi.org/10.1038/nature01292)
- Lellouch, E., Strobel, D. F., Belton, M. J. S., et al. 1996, *ApJL*, 459, L107, doi: [10.1086/309956](https://doi.org/10.1086/309956)
- Lellouch, E., Gurwell, M. A., Moreno, R., et al. 2019, *Nature Astronomy*, 3, 614, doi: [10.1038/s41550-019-0749-4](https://doi.org/10.1038/s41550-019-0749-4)
- McDoniel, W. J., Goldstein, D. B., Varghese, P. L., & Trafton, L. M. 2015, *Icarus*, 257, 251, doi: [10.1016/j.icarus.2015.03.019](https://doi.org/10.1016/j.icarus.2015.03.019)
- . 2017, *Icarus*, 294, 81, doi: [10.1016/j.icarus.2017.04.021](https://doi.org/10.1016/j.icarus.2017.04.021)
- . 2019, *Physics of Fluids*, 31, 077103, doi: [10.1063/1.5097961](https://doi.org/10.1063/1.5097961)
- McMullin, J. P., Waters, B., Schiebel, D., Young, W., & Golap, K. 2007, in *Astronomical Society of the Pacific Conference Series*, Vol. 376, *Astronomical Data Analysis Software and Systems XVI*, ed. R. A. Shaw, F. Hill, & D. J. Bell, 127
- Moore, C. H. 2011, PhD thesis, University of Texas, Austin
- Moore, C. H., Goldstein, D. B., Varghese, P. L., Trafton, L. M., & Stewart, B. 2009, *Icarus*, 201, 585, doi: [10.1016/j.icarus.2009.01.006](https://doi.org/10.1016/j.icarus.2009.01.006)
- Morabito, L. A., Synnott, S. P., Kupferman, P. N., & Collins, S. A. 1979, *Science*, 204, 972, doi: [10.1126/science.204.4396.972](https://doi.org/10.1126/science.204.4396.972)
- Moreno, M. A., Schubert, G., Baumgardner, J., Kivelson, M. G., & Paige, D. A. 1991, *Icarus*, 93, 63, doi: [10.1016/0019-1035\(91\)90164-O](https://doi.org/10.1016/0019-1035(91)90164-O)
- Moulet, A., Gurwell, M. A., Lellouch, E., & Moreno, R. 2010, *Icarus*, 208, 353, doi: [10.1016/j.icarus.2010.02.009](https://doi.org/10.1016/j.icarus.2010.02.009)
- Moulet, A., Lellouch, E., Moreno, R., et al. 2013, *ApJ*, 776, 32, doi: [10.1088/0004-637X/776/1/32](https://doi.org/10.1088/0004-637X/776/1/32)
- Moulet, A., Lellouch, E., Moreno, R., Gurwell, M. A., & Moore, C. 2008, *A&A*, 482, 279, doi: [10.1051/0004-6361:20078699](https://doi.org/10.1051/0004-6361:20078699)
- Müller, H. S. P., Schlöder, F., Stutzki, J., & Winnewisser, G. 2005, *Journal of Molecular Structure*, 742, 215, doi: [10.1016/j.molstruc.2005.01.027](https://doi.org/10.1016/j.molstruc.2005.01.027)
- Müller, H. S. P., Thorwirth, S., Roth, D. A., & Winnewisser, G. 2001, *A&A*, 370, L49, doi: [10.1051/0004-6361:20010367](https://doi.org/10.1051/0004-6361:20010367)
- Pearl, J., Hanel, R., Kunde, V., et al. 1979, *Nature*, 280, 755, doi: [10.1038/280755a0](https://doi.org/10.1038/280755a0)
- Redwing, E., de Pater, I., Luszcz-Cook, S., et al. 2022, *PSJ*, 3, 238, doi: [10.3847/PSJ/ac9784](https://doi.org/10.3847/PSJ/ac9784)
- Roth, L., Boissier, J., Moulet, A., et al. 2020, *Icarus*, 350, 113925, doi: [10.1016/j.icarus.2020.113925](https://doi.org/10.1016/j.icarus.2020.113925)
- Schneider, N. M., & Spencer, J. R. 2023, in *Astrophysics and Space Science Library*, Vol. 468, *Io: A New View of Jupiter's Moon*, ed. R. M. C. Lopes, K. de Kleer, & J. T. Keane, 9–39, doi: [10.1007/978-3-031-25670-7_2](https://doi.org/10.1007/978-3-031-25670-7_2)
- Sicardy, B. 2023, *Comptes Rendus Physique*, 23, 213, doi: [10.5802/crphys.109](https://doi.org/10.5802/crphys.109)
- Simon, A. A., Wong, M. H., Sromovsky, L. A., Fletcher, L. N., & Fry, P. M. 2022, *Remote Sensing*, 14, 1518, doi: [10.3390/rs14061518](https://doi.org/10.3390/rs14061518)
- Spencer, J. R., Lellouch, E., Richter, M. J., et al. 2005, *Icarus*, 176, 283, doi: [10.1016/j.icarus.2005.01.019](https://doi.org/10.1016/j.icarus.2005.01.019)
- Tsang, C. C. C., Spencer, J. R., & Jessup, K. L. 2013a, *Icarus*, 226, 604, doi: [10.1016/j.icarus.2013.06.010](https://doi.org/10.1016/j.icarus.2013.06.010)

- . 2015, *Icarus*, 248, 243,
doi: [10.1016/j.icarus.2014.10.033](https://doi.org/10.1016/j.icarus.2014.10.033)
- Tsang, C. C. C., Spencer, J. R., Lellouch,
E., Lopez-Valverde, M. A., & Richter,
M. J. 2016, *Journal of Geophysical
Research (Planets)*, 121, 1400,
doi: [10.1002/2016JE005025](https://doi.org/10.1002/2016JE005025)
- Tsang, C. C. C., Spencer, J. R., Lellouch,
E., et al. 2012, *Icarus*, 217, 277,
doi: [10.1016/j.icarus.2011.11.005](https://doi.org/10.1016/j.icarus.2011.11.005)
- . 2013b, *Icarus*, 226, 1177,
doi: [10.1016/j.icarus.2013.06.032](https://doi.org/10.1016/j.icarus.2013.06.032)
- Walker, A. C. 2012, PhD thesis,
University of Texas, Austin
- Walker, A. C., Gratiy, S. L., Goldstein,
D. B., et al. 2010, *Icarus*, 207, 409,
doi: [10.1016/j.icarus.2010.01.012](https://doi.org/10.1016/j.icarus.2010.01.012)
- Walker, A. C., Moore, C. H., Goldstein,
D. B., Varghese, P. L., & Trafton, L. M.
2012, *Icarus*, 220, 225,
doi: [10.1016/j.icarus.2012.05.001](https://doi.org/10.1016/j.icarus.2012.05.001)